doi: 10.1093/pasj/xxx000

Dark supernova remnant buried in the Galactic-Centre "Brick" G0.253+0.016 revealed by an expanding CO-line bubble

Yoshiaki SOFUE[1]

[1]Institute of Astronomy, The University of Tokyo, Mitaka, Tokyo 183-0015, Japan

*E-mail: sofue@ioa.s.u-tokyo.ac.jp

Received ; Accepted

Abstract

We performed a ^{12}CO - and ^{13}CO -line study of the "Brick" (G0.253+0.016) in the Galactic Centre (GC) by analyzing the archival data obtained with the Nobeyama 45-m telescope. We present kinematics and molecular gas distributions in the longitude-velocity diagram, and suggest that the Brick is located along the GC Arm I in the central molecular zone (CMZ) in front of the GC, which yields a distance of 8 kpc and GC radius 0.2 kpc. The major and minor-axis diameters of the Brick are $D_x \times D_y = 8.4\mathrm{pc} \times 4.1\mathrm{pc}$ at position angle of 40° and 130°, respectively, and the scale radius is $r_{\rm Bri} = \sqrt{D_x D_y} = 2.96\mathrm{pc}$. The molecular mass inferred from the ^{12}CO -line integrated intensity is $M_{\rm Bri;Xco} \sim 5.1 \times 10^4 M_\odot$. for a conversion factor $X_{\rm CO;GC} = 1.0 \times 10^{20}$ $\mathrm{H_2}$ cm $^{-2}$ [K km s^{-1}]$^{-1}$, a half of the local value. On the other hand, the dynamical (Virial) mass for the measured velocity dispersion of $\sigma_v = 10.0\mathrm{km\ s^{-1}}$ is calculated to be $M_{\rm Bri;vir} \sim 6.8 \times 10^4 M_\odot$, which yields a new conversion factor of $X_{\rm CO;Bri} = 1.3 \times 10^{20}$ $\mathrm{H_2}$ cm $^{-2}$ [K km s^{-1}]$^{-1}$. No thermal radio emission indicative of HII region and present star formation (SF) is found in radio-continuum archive. The Brick's center has a cavity surrounded by a spherical molecular bubble of radius $r_{\rm bub} = 1.85$ pc and mass $\sim 1.7 \times 10^4 M_\odot$ expanding at $v_{\rm exp} = 10\mathrm{km\ s^{-1}}$ with kinetic energy of $E_0 \sim 1.7 \times 10^{49}$ erg. If the bubble is approximated by an adiabatic spherical shock wave, its age is estimated to be $t \sim 2/5 r_{\rm bub}/v_{\rm exp} \sim 7.2 \times 10^4$ y. We suggest that the bubble will be a dark supernova remnant buried in the dense molecular cloud. The Brick, therefore, experienced massive-star formation followed by a supernova explosion more than $\sim 10^5$ y ago.

Key words: Galaxy: centre — ISM: bubbles — ISM: clouds — ISM: molecules — ISM: supernova remnant

1 Introduction

The "Brick" (G0.253+0.016, M0.25+0.01) near the Galactic Center (GC) is a dense dust cloud detected in the sub-mm continuum emission (Guesten & Henkel 1983; Lis et al. 1994; Johnston et al. 2014). Sub-mm wave photometry indicated column density of molecular gas as high as $\sim 10^{23}$ $\mathrm{H_2 cm^{-2}}$ and mass of $\sim 1.5 \times 10^5 M_\odot$ (Longmore et al. 2012). It exhibits heavy extinction in infrared wavelengths silhouetted against the central stellar disc and bulge (Henshaw et al. 2019; Ginsburg et al. 2023). The cloud is detected in the molecular lines at radial velocity $v_{\rm LSR} \sim 30\mathrm{km\ s^{-1}}$ (Johnston et al. 2014; Lis & Carlstrom 1994). Interferometer observations with ALMA (Atacama Large Millimeter and submillimeter Array) have revealed a bubble/cavity structure near the center of the Brick, which exhibits a half-loop structure composed of a number of filamentary arcs concentric to the bubble center (Higuchi et al. 2014; Henshaw et al. 2022).

There have been two models to explain the bubble/arc

© 2018. Astronomical Society of Japan.

structure: One idea is that it is a cavity produced by a collision of a compact molecular cloud at high speed from high-latitude direction (Higuchi et al. 2014). The other attributes the bubble to stellar feedback such as a wind from young stars (Johnston et al. 2014; Henshaw et al. 2019; Henshaw et al. 2022). While signature of star formation has been found by detection of maser lines and outflow from young stars (Lis et al. 1994; Longmore et al. 2012; Walker et al. 2021), no clear evidence is yet reported of HII regions indicative of massive-star formation (Anderson et al. 2014; Wenger et al. 2023).

Infrared photometry of the bulge stars and extinction study indicated a distance of ~ 7 kpc (Longmore et al. 2012; Zoccali et al. 2021), locating the cloud about 1 kpc in front of the GC. On the other hand, extinction study of GC stars with known proper motions suggested that the Brick is inside the central molecular zone (CMZ) in front of the GC disc stars (Martínez-Arranz et al. 2022).

In this paper we study the kinematics and energetics of the Brick by analyzing the CO-line data from the GC survey with the Nobeyama 45-m mm-wave telescope (Tokuyama et al. 2019). We argue that the Brick is more likely to be associated with the CMZ located at a distance of ~ 8 kpc. We derive the fundamental physical parameters such as the size, mass, kinetic and gravitational energies of the Brick based on the Nobeyama ^{12}CO - and ^{13}CO -line data, which, because of the single-dish aperture, do not suffer from the missing-mass problem in interferometric measurments. So, the present study will be complimentary to the current interferometer works in the sense that the present analysis provides with information more about physics that has not been explored in the current studies, while it does not add much information about the detailed morphology in the cloud.

We then focus on the expanding molecular bubble centered on $(l, b) = (0^\circ.253, +0^\circ.016)$ (G0.253+0.016), and present a new model attributing it to a dark supernova remnant (SNR) buried in the dense molecular Brick (Shull 1980; Wheeler et al. 1980; Sofue 2020; Sofue 2021) in order to explain the kinetic energy an order of magnitude greater than that estimated from the interferometer observations.

2 The Brick in the CO line

2.1 CO-line data

We use the CO-line survey of the Galactic Center using the Nobeyama 45-m telescope (Tokuyama et al. 2019), which cover the GC region for $1^\circ.4 \times 0^\circ.8$ in the ^{12}CO and ^{13}CO line emissions. The full width of half maximum of the telescope beam was $15''$ and $16''$, respectively, corresponding to 0.60 and 0.64 pc at the GC distance of 8.2 kpc. The data cubes have grid sizes of $7''.5 \times 7''.5 \times 2$km s^{-1}. Both bands were observed simultaneously, and the rms noise in the data cube was ~ 0.2 K.

2.2 Intensity distribution: moment 0 map

Figure 1 shows integrated intensity (moment 0) maps in the ^{13}CO line emission between $v_{\rm LSR} = 0$ and 60 km s^{-1}for a $0^\circ.5 \times 0^\circ.4$ (top panel) and $0^\circ.16 \times 0^\circ.16$ (middle) regions around the Brick. The middle panel is drawn by contours overlaid on the Spitzer (GLIMPSE) 8 μm intensity map in grey-scaling (Churchwell et al. 2009). The map shows tight correlation of the CO cloud in emission with the dust Brick in silhouette against the stellar background of the central bulge and GC stellar disk. The bottom panel shows perpendicular cross sections of the Brick along the dashed line in the middle panel, showing plateaued intensity profiles both in infrared and ^{13}CO indicative of density cavity inside the brick as will be discussed later based on channel maps and position-velocity diagrams.

Figure 2 shows integrated intensity (moment 0) maps of the ^{12}CO and ^{13}CO line emissions of the Brick along with a velocity field (moment 1) and velocity dispersion map (moment 2). The ^{12}CO map shows a slightly smoother distribution than the map in ^{13}CO despite of the sharper beam because of the broader distribution as well as more sensitive detection of extended and diffuse gas clouds. The bottom panel shows the cross section of the ^{13}CO intensity perpendicular to the Brick's major axis (position angle $\sim 130^\circ$) across the map center of the middle panel. The plateaued intensity distributions both in the infrared absorption and CO emission indicate a cavity inside the cloud, unless the brick is cubicle shaped.

2.3 Velocity gradient and dispersion: moment 1 and 2 maps

Figure 2 shows moment 1 and 2 maps, showing the mean-velocity field and velocity dispersion distributions. The velocity field indicates a gradual increase in the radial velocity from NE to SW. The gradient may be attributed to rotation of the cloud around the minor axis of the Brick. Then, the rotation is nearly rigid with an angular speed of 2.5 km s^{-1}pc^{-1} and the rotation period is ~ 2.5 My.

The moment 2 map shows a maximum of $\sigma_v \sim 13$ km s^{-1}near the map center and generally ~ 10km s^{-1} over the Brick, which will be used later to estimate the velocity dispersion of the cloud for calculating the dynamical mass and kinetic energy.

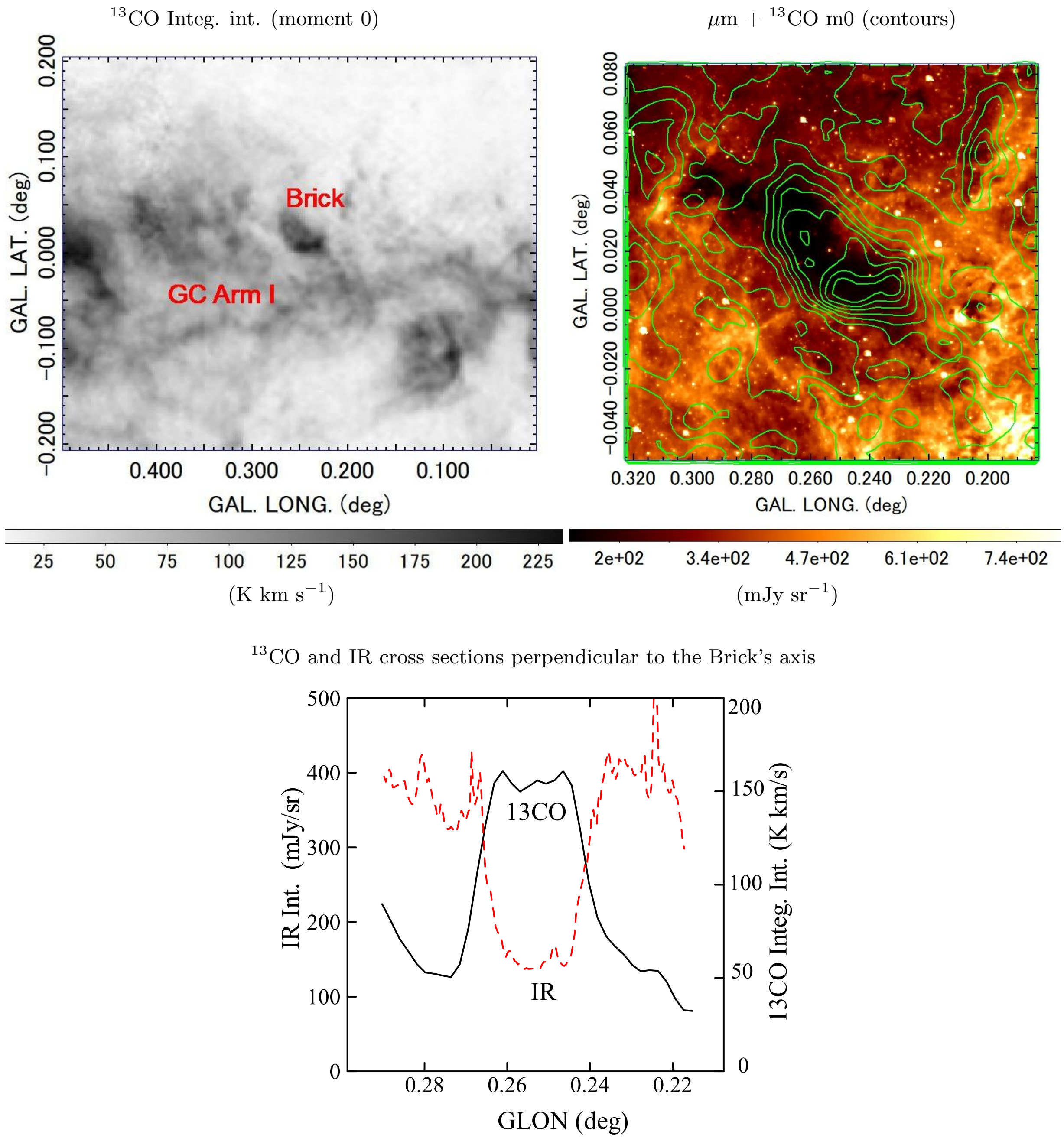

Fig. 1. [Top left] ^{13}CO intensity (moment 0) map integrated from $v_{\rm LSR}=0$ to 60 km s^{-1} around the Brick. [Top right] The Brick in ^{13}CO intensity by contours every 20 K km s^{-1} overlaid on the Spitzer (GLIMPSE) 8 μm intensity map (grey scale in mJy/sr) (Churchwell et al. 2009), showing coincidence of CO and dust clouds. [Bottom] ^{13}CO intensity profiles (black line) and 8 μm (dashed line) perpendicular to the Brick's major axis across $(l,b)=0^\circ.253, +0^\circ.016)$.

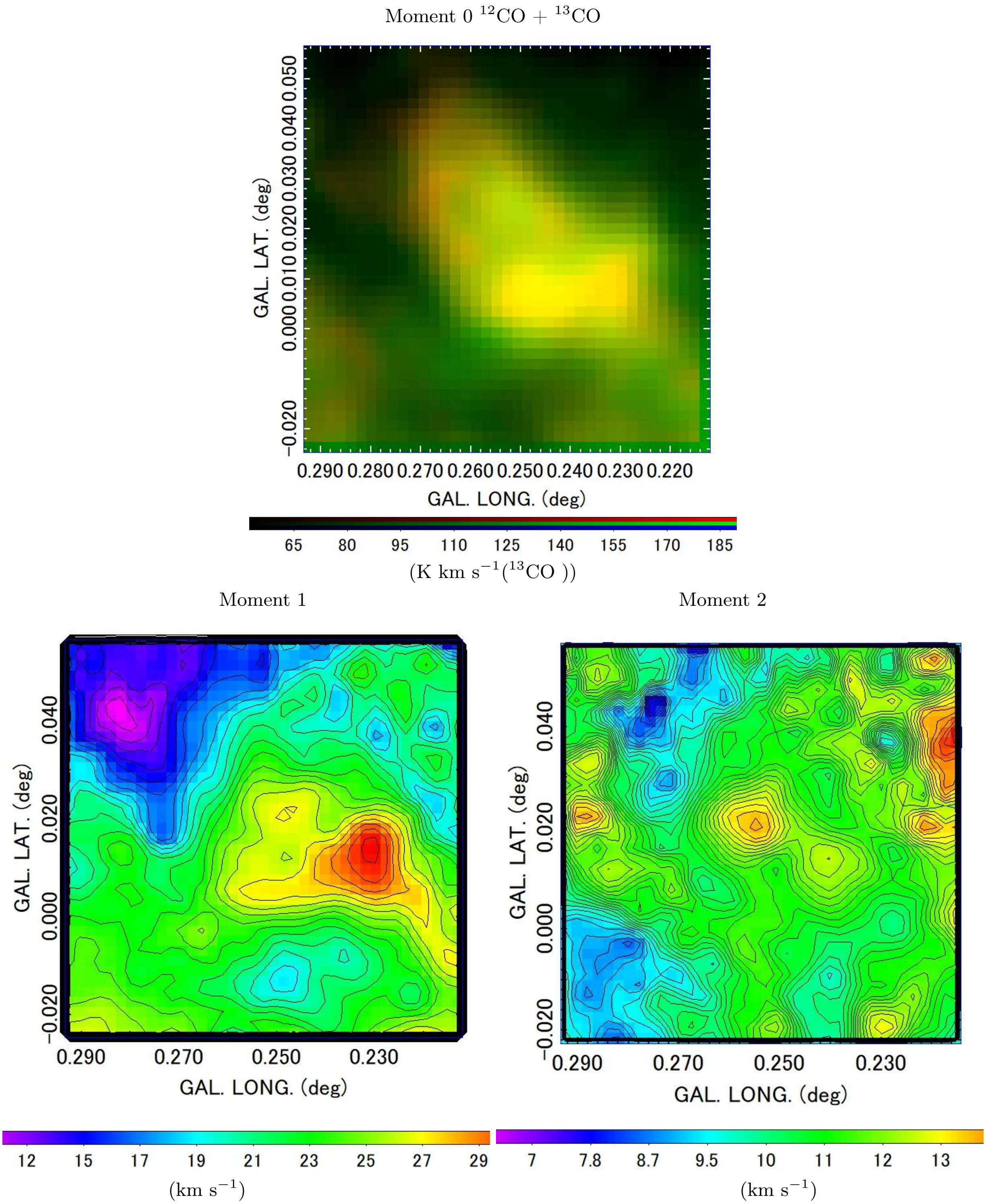

Fig. 2. [Top] Composite map of integrated intensities from 0 to 60 km s^{-1}in the ^{12}CO (green: from 250 to 1250 K km s^{-1}) and ^{13}CO (red: 50 to 250) lines. [bottom] Moment 1 (velocity field) and 2 (dispersion) in km s^{-1}.

2.4 Channel maps

Figure 3 shows channel maps of the brightness temperature $T_{\rm B}$ of the ^{13}CO emission around the Brick from $v_{\rm LSR}=21$ to 43 km s^{-1}. The maps show ring-like distributions of the brightness making a cavity in the central region. The ring feature at velocity ~ 30 km s^{-1}slice is well fitted by a circle representing the cross section of a spherical bubble (shell) centered on $(l,b)=(0^\circ.253,+0^\circ.016)$ with radius $\sim 1'.6$ (1.7 to 1.9 pc at $d=7.2$ to 8 kpc). The bubble is associated with a peaky clump in the SW edge. Combining with elliptical features in the position-velocity diagrams, this ring will be attributed to an expanding molecular shell (bubble) in the following subsections.

2.5 Position-velocity diagrams

In figures 4 and 5 we show longitude-velocity diagrams (LVD) sliced at various latitudes and latitude-velocity digrams (BVD) sliced at various longitudes, respectively. In both diagrams, elliptical features are recognized as marked by the red circles, indicating a bubble structure expanding at velocity of $v_{\rm expa}\sim 10$ km s^{-1}.

Figure 6 shows LVDs in wider area across G0.253+0.016 at a constant latitude $b=0^\circ.016$, covering the central molecular zone (CMZ) (top panel) and close up (bottom). The prominent ridge running from top left to bottom right represents the Galactic Center Arm I and the fainter one at higher velocities is Arm II (Sofue 1995). The Brick is recognized as a clump at a systemic velocity of $v_{\rm LSR}=30$ km s^{-1}ranging from ~ 20 to 40 km s^{-1}. The Brick is located in touch but slightly displaced from GC Arm I. This will be used later for discussing the distance of the Brick, while kinematic distance using the Galactic rotation is not applied here because of the nearly zero longitude,

3 Distance and kimenatics

3.1 Distance and location in the CMZ

Extinction study of the bulge stars in infrared indicated a distance of $d=7.2\pm 0.2$ kpc, locating the cloud in front of the central bulge (Zoccali et al. 2021). On the other hand, extinction of stars with known proper motion indicated the location inside the CMZ (Martínez-Arranz et al. 2022).

If $d\sim 7$ kpc, the Galacto-centric distance of the Brick is $R\sim 1.0$ kpc. In order to see if the 1 kpc region is rich enough in the molecular gas for nesting such a dense cloud as the Brick, we examined an LVD from the Columbia 1.2-m CO-line survey (Dame et al. 2001) in the central region at $l\sim\pm 7^\circ$ ($R=R_0\sin l\sim 1$ kpc). We immediately found that the ring region at $R\sim 1$ kpc is almost empty in the LVD. Next, we examined the LVD of the CMZ in figure 6, where we do not also find any LV feature parallel to the straight dashed line with gradient $dv/dl\sim 30$ km s^{-1}degree^{-1} representing a supposed 1-kpc ring or arm rotating at ~ 200 km s^{-1}. Therefore, it is difficult to attribute the Brick to a molecular disc or ring in the Galactic plane with radius $R\sim 1$ kpc, unless a completely isolated dense cloud is orbiting alone in such an empty region and is by chance observed exactly in the GC direction.

On other hand, the LVD in figure 6 suggests that the Brick is more closely correlated with the CMZ, which is composed of dense and clumpy molecular arms (GC Arms I and II) running at steeper slopes of $dv/dl\sim 150$ km s^{-1}degree^{-1}. It is stressed that the systemic velocity of the Brick (~ 30 km s^{-1}) is different only by +10 km s^{-1}from the ridge velocity at $v_{\rm LSR}=+20$ km s^{-1}of Arm I at $l\sim 0^\circ.25$, safely within the velocity dispersion of the CMZ molecular gas. In fact, Arm I is full of clumpy clouds whose velocity displacements are $\sim\pm 20$ km s^{-1}with the extreme case of ~ -30km s^{-1} of the Sgr B molecular complex.

It seems, therefore, more reasonable to consider that the Brick is an object physically associated with the CMZ rather than to locate it at 1 kpc away from the GC. We, therefore, assume hereafter that the Brick is located inside the CMZ associated with GC Arm I. Because Arm I composes a ring of radius $R\sim 160$ pc (Sofue 2022), the distance to the Brick is $d=8$ kpc from the Sun for the GC (Sgr A$*$) distance $R_0=8.2$ kpc. This assumption is in agreement with the extinction study of stars with known proper-motions that located the Brick in the CMZ but in front of the centre (Martínez-Arranz et al. 2022). However, the shorter distance cannot be excluded totally at the present.

3.2 On the heavy extinction

We comment on the heavier extinction of the Brick than that of Sgr B molecular complex despite comparable or higher gas density in the latter. Since the Brick is at $0^\circ.25$ from the GC, it is a silhouette against the central core of the stellar bulge near $R\sim 35$ pc. On the other hand, Sgr B at $l\sim 0^\circ.6$ is silhouetted against the bulge stars at $R\sim 86$ pc. It is known that the central stellar mass distribution is expressed by two components: one is the central bulge with scale radius 120 pc and central stellar density $2\times 10^2 M_\odot$ pc^{-3}, and the other is the inner bulge or core which has the scale radius of 38 pc and center density $4\times 10^4 M_\odot$ pc^{-3} (Sofue 2013). The difference of the distances of the clouds from the GC on the sky, 35 and 86 pc, therefore, yields a significant difference of the background infrared brightness with or without the inner bulge. This results in much

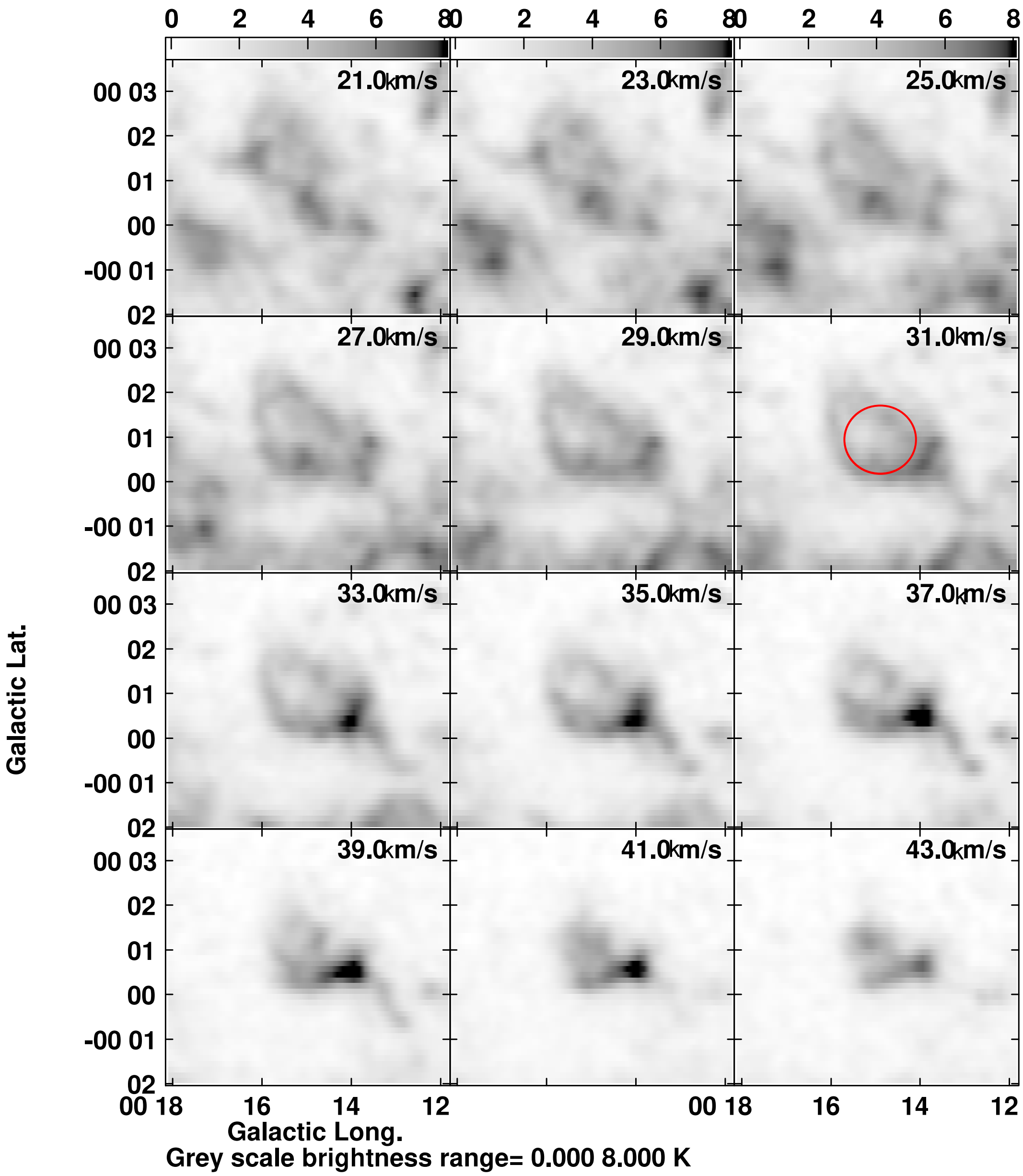

Fig. 3. Channel maps of ^{13}CO $T_{\rm B}$ (K by bar) of the Brick every 2 km s^{-1}interval of $v_{\rm LSR}$. Note the ring-like distribution of the emission, indicating a shell structure. Red circle marks the bubble of radius 1.9 pc (at 8 kpc) centered on $(l,b)=(0^\circ.253,+0^\circ.016)$ with radius 1.9 pc. Note tht coordinate values are in unit of $dd^\circ\ mm'$.

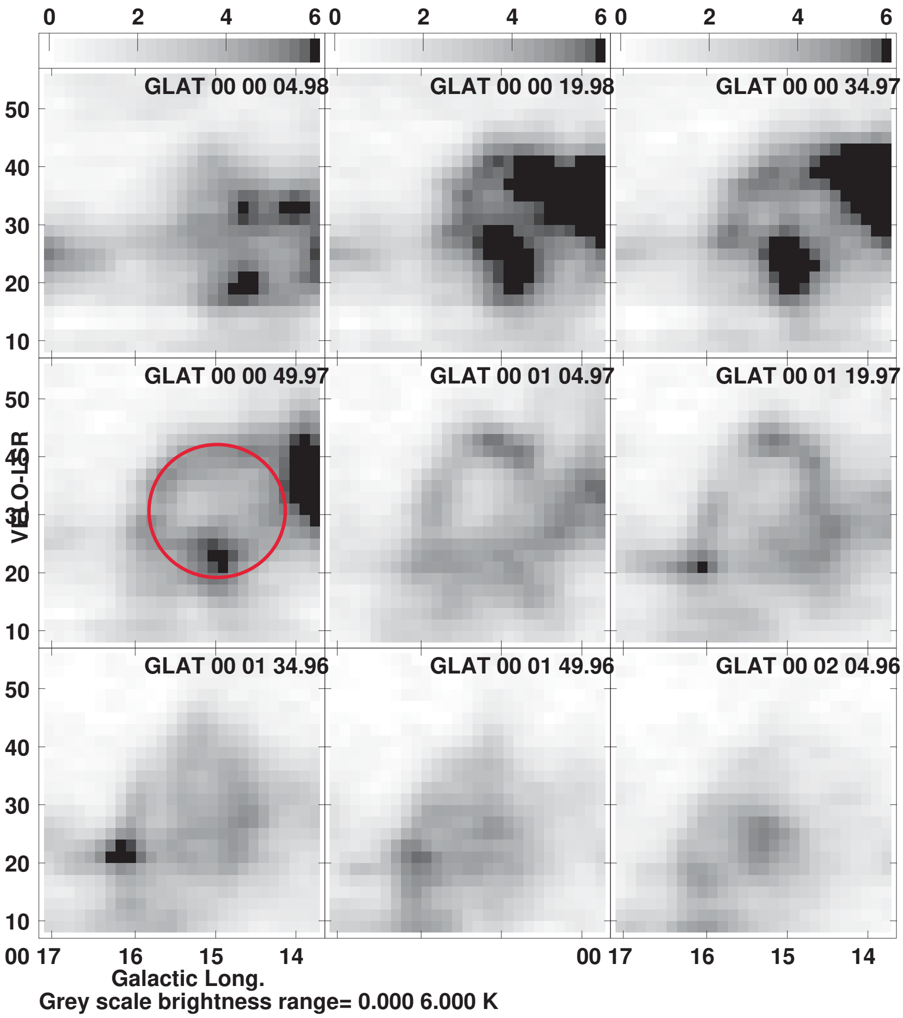

Fig. 4. LVDs at various latitudes. Red circle traces the LV ellipse representing the expanding bubble at 10 km s^{-1}. Note: Coordinate values are in unit of $dd^\circ\ mm'$ and km s^{-1}and labels in unit of $dd^\circ\ mm'\ ss''$.

brighter background toward the Brick $\gtrsim 10^2$ times than for Sgr B, and explains the particularly heavy extinction measured in absolute brightness toward the Brick.

3.3 Size of the Brick

We use the moment maps to measure the fundamental parameters for calculating the kinematical parameters such as the size, molecular mass, kinematic and gravitational energies, the density, and time scale of the cloud. Figure 7 shows the ^{12}CO -line moment 0 map, where the measured sizes in the ^{13}CO map is shown by the arrows, and the area for luminosity measurement by red line and off-source regions by dashed line.

The derived parameters are listed in table 1. FWHM (full width of half maximum) sizes (diameters) $D_x = 0^\circ.060$ and $D_y = 0^\circ.030$ in the major and minor axial directions, respectively, of the Brick were measured by reading the coordinates at the steepest sides of the ^{13}CO -line profiles, which have both plateaued shapes. We thus obtain $D_x = 8.43$ and $D_y = 4.13$ pc, respectively, for $d = 8$ kpc, and the size radius

$$r = \sqrt{D_x D_y}/2 = 2.96 \text{ pc}. \tag{1}$$

This size is slightly larger than that measured on the dust emission map of 2.7 pc for a distance of 8 kpc (originally 2.8 pc for a distance of 8.4 kpc) (Longmore et al. 2012).

3.4 Molecular mass by ^{12}CO -to-H$_2$ conversion

We first calculate the molecular mass using the conversion factor derived for the GC region of $X_{\rm CO} = 1.0 \times 10^{20}$ H$_2$ cm^{-3} [K km s^{-1}]$^{-1}$ (Arimoto et al. 1996) and the nominal molecular weight of $\mu = 1.38$. Using ^{12}CO moment 0 map shown in figure 7 we measured the surface-integrated line intensity of the area enclosed by the red line. We also mea-

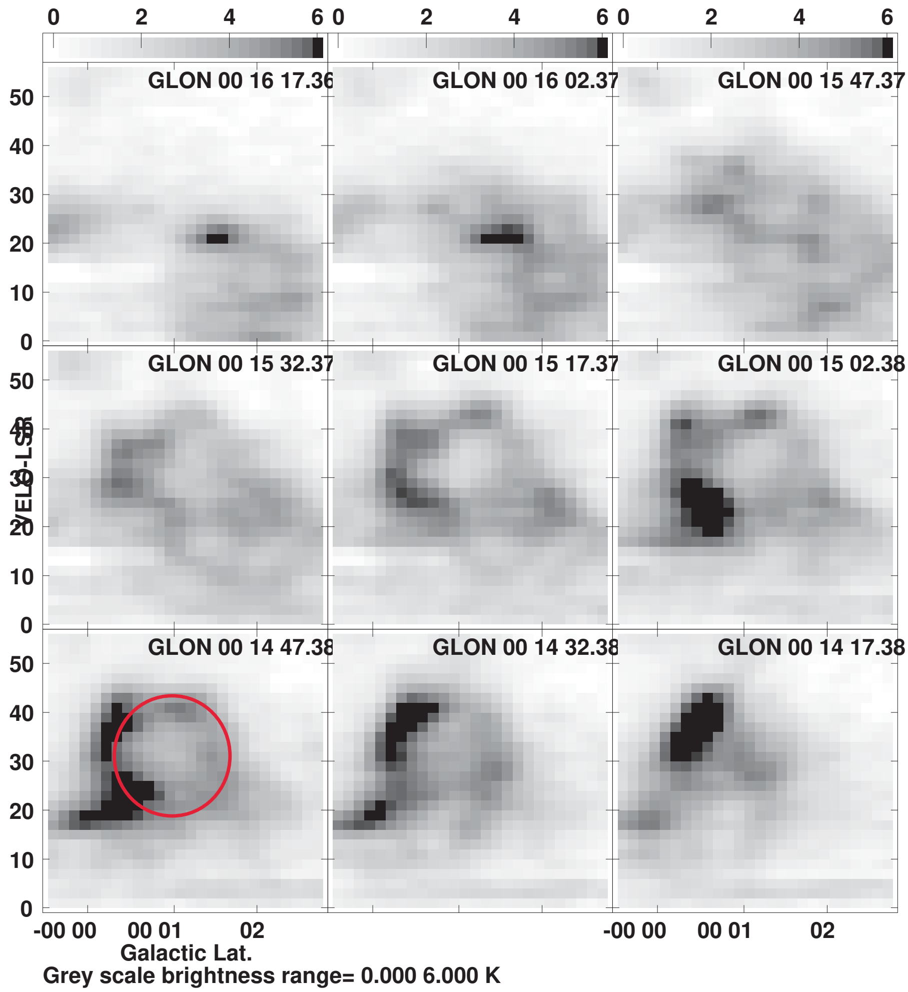

Fig. 5. BVDs. The red circle indicates the expanding bubble. Note: Coordinate values are in unit of $dd^\circ\ mm'$ and km s^{-1} and labels in unit of $dd^\circ\ mm'\ ss''$.

sured the off-source mean intensity in the area enclosed by the dashed line. By subtracting the corresponding surface-integrated intensity of the base level from the on-source value, we obtain the ^{12}CO luminosity of the Brick,

$$L_{12\mathrm{CO}} = 2.21\times10^{41}\mathrm{K\ km\ s^{-1}cm^{2}}. \quad (2)$$

The total molecular-gas mass is then obtained to be

$$M_{\mathrm{Bri;Xco}} = X_{\mathrm{CO}} L_{12\mathrm{CO}} (2\mu m_{\mathrm{H}}) = 5.1\times10^{4} M_{\odot}. \quad (3)$$

The mean molecular-gas density is calculated by

$$\rho = M_{\mathrm{Bri;Xco}}/(4\pi r^3/3) = 3.3\times10^{-20}\mathrm{g\ cm^{-3}}, \quad (4)$$

or

$$n_{\mathrm{H_2}} = 6.5\times10^{3}\ \mathrm{H_2\ cm^{-3}}. \quad (5)$$

The Jeans (free fall) time in the cloud is estimated to be

$$t_{\mathrm{J}} = 1/\sqrt{4\pi G\rho} \sim 0.19\ \mathrm{My} \quad (6)$$

for zero sound velocity limit. We also measured the peak intensity to be $I_{\mathrm{CO}} = 660$ Kkms, and the $\mathrm{H_2}$ column density at the brightest clump to be $N_{\mathrm{H_2}} = X_{\mathrm{CO}} I_{\mathrm{CO}} = 6.6\times10^{22}$ $\mathrm{H_2\ cm^{-2}}$.

3.5 The Virial mass

The dynamical quantities can be estimated from the obtained CO kinematic quantities. Using the moment 2 map we measure the velocity dispersion to be $\sigma_{\mathrm{cen}} = 13$km s^{-1} near the cloud center and $\sigma_{\mathrm{v}} = 10$ km s^{-1} over the entire cloud. Since the central high dispersion may be influenced by the expanding bubble, as discussed later, we here adopt the overall value for the dispersion of the cloud. We here use mean velocity dispersion to calculated dynamical (Virical) mass as

$$M_{\mathrm{Bri;vir}} = r\sigma_v^2/G \sim 6.8\times10^{4} M_{\odot}. \quad (7)$$

The density for this Virial mass is then calculated by

$$\rho = M_{\mathrm{vir}}/(4\pi r^3/3) = 4.3\times10^{-20}\mathrm{g\ cm^{-3}}, \quad (8)$$

or

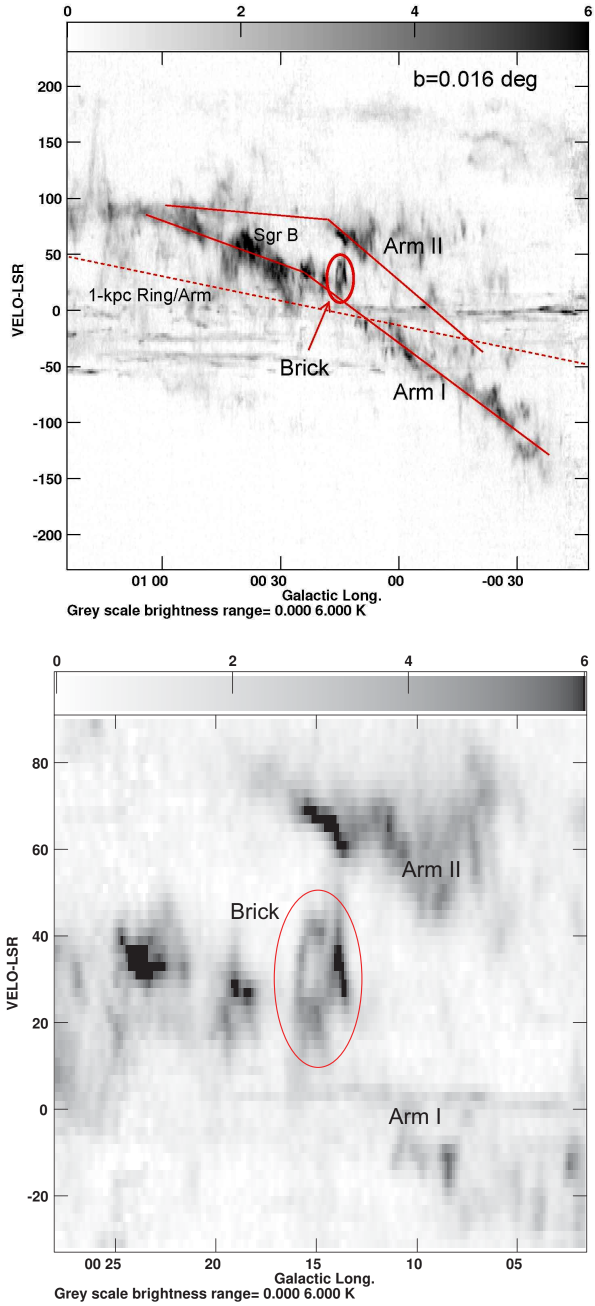

Fig. 6. [Top] LVD of the ^{13}CO line across the center of Brick along $b = 0^\circ.016$. The Brick shows up as a clump at $l = 0^\circ.253$ and $v_{\rm LSR} \simeq 30$ km s^{-1}between the GC Arm I and II (red lines) (Sofue 1995). Dashed line indicates a possible arm of galacto-centric radius 1 kpc on which the Brick might be located, if the distance is ~ 7 kpc, but it does not exist. [Bottom] Same, but close up. Note: In both panels, the horizontal-coordinate unit is $dd^\circ\ mm'$.

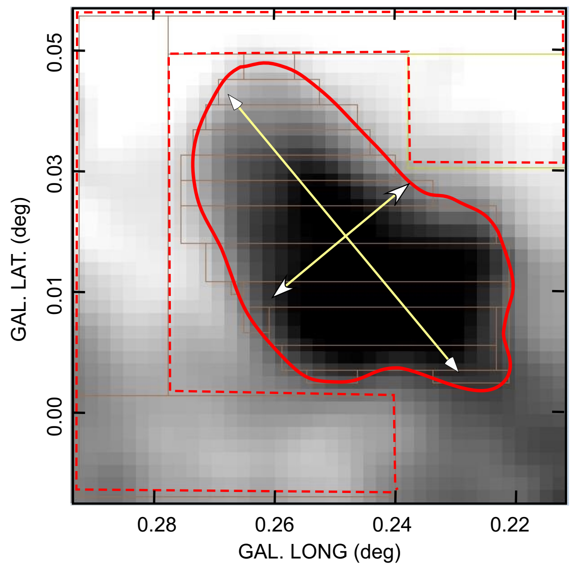

Fig. 7. ^{12}CO moment 0 map of the Brick. The arrows indicate major and minor-axial diameters (D_x, D_y) as read on the ^{13}CO -line moment 0 map. Red line encloses the area for the ^{12}CO -luminosity measurement in order to determine the molecular mass using the conversion factor. The dashed line encloses the area used to calculate the base level.

$$n_{\rm H_2} = 8.7 \times 10^3\ {\rm H_2\ cm^{-3}}. \tag{9}$$

The free-fall (Jeans) time of the cloud center is estimated to be

$$t_{\rm J} = 1/\sqrt{4\pi G\rho} \sim 0.17\ {\rm My}. \tag{10}$$

Thus obtained total flux of the ^{12}CO intensity was converted to the luminosity at a distance of 8 kpc, and converted to the molecular-gas mass by

$$M_{\rm brick} = X_{\rm CO} I_{\rm CO} A \times (2 m_{\rm H} \mu) \tag{11}$$

where A is the area of the Brick and $\mu = 1.38$ is the mean atomic weight. Adopting $X_{\rm CO} = 1.0 \times 10^{20}$ H$_2$ cm $^{-2}$ [K km s^{-1}]$^{-1}$, we obtain $M_{\rm Bri;vir} = 5.1 \times 10^4 M_\odot$.

The kinetic energy of the Brick corresponding to this Virial mass is $E_{\rm k} = 1/2 M_{\rm vir} \sigma_v^2 \sim 0.68 \times 10^{50}$ erg. The gravitational energy is estimated by $E_{\rm g} = G M_{\rm mol}^2 / r \sim 1.37 \times 10^{50}$ erg, trivially satisfying $2E_{\rm k} - E_{\rm g} \sim 0$.

3.6 Comment on the conversion factor and gas-to-dust mass ratio

The Virial mass is therefore 1.6 times greater than the molecular mass for the conversion factor in the GC of $Xco^{\rm GC} = 1.0 \times 10^{20}$ H$_2$ cm $^{-2}$ [K km s^{-1}]$^{-1}$. This means either that the cloud is not Virialized, or that the conversion factor is wrong. If the former is the case and the cloud is unstable and being disrupted, its age must be as short as

Table 1. Kinematic properties of the Brick G0.253+0.016 and the bubble.

Parameter	Result	Remark
Brick: observed quantities		
Distance $d = R_0 - 0.2$ kpc	8 kpc	On GC Arm I in front of Sgr A*
Approximate centre $(l, b, v_{\rm LSR})$	$(0^\circ.249,\ 0^\circ.020,\ +30{\rm km\ s^{-1}})$	Figure 7
Major diameter (PA=40°) D_x	$0^\circ.060 = 8.43$pc	^{13}CO mom. 0 map, figure 7
Minor diameter (PA=130°)D_y	$0^\circ.030 = 4.12$pc	ibid
Size radius $r = \sqrt{D_x D_y}/2$	2.96 pc	
Velocity dispersion σ_v	10 km s^{-1}	
^{12}CO Peak intensity $I_{^{12}{\rm CO}}$	660 K km s^{-1}	
^{12}CO Mean intensity $I_{^{12}{\rm CO}}$	430 K km s^{-1}	Figure 7
$X_{\rm CO}$ mass		
Mass mol. $M_{\rm Bri;Xco}$	$5.1 \times 10^4 M_\odot$	^{12}CO m0 aperture photo.
Conversion factor $X_{\rm CO}^{\rm GC}$	1.0×10^{20} H$_2$ cm $^{-2}$ [K km s^{-1}]$^{-1}$	GC conv. factor (Arimoto et al. 1996)
$\rho_0 = M_{\rm Bri;Xco}/(\frac{4\pi}{3} r^3)$	3.3×10^{-20} g cm^{-3} $(= 7.2 \times 10^3\ {\rm H_2\ cm^{-3}})$	For $X_{\rm CO}^{\rm GC}$ mass
Energy, kinetic: $E_k = M_{\rm Bri;Xco}\sigma_v^2/2$	0.51×10^{50} erg	
Energy, gravi: $E_g = GM_{\rm Bri;Xco}^2/r$	0.76×10^{50} erg	
$t_{\rm ff} = 1/\sqrt{4\pi G\rho}$	0.19 My	
Virial mass		
Mass Virial: $M_{\rm Bri;vir} = r\sigma_v^2/G$	$6.8 \times 10^4 M_\odot$	Virial mass
New conversion factor $X_{\rm CO;Bri}$	1.3×10^{20} H$_2$ cm $^{-2}$ [K km s^{-1}]$^{-1}$	$X_{\rm CO;Bri}$ mass = Virial mass
$\rho_0 = M_{\rm Bri;vir}/(\frac{4\pi}{3} r^3)$	4.3×10^{-20} g cm^{-3} $(= 9.3 \times 10^3\ {\rm H_2\ cm^{-3}})$	ibid
Energy kinetic: $E_{\rm k} = M_{\rm Bri;vir}\sigma_v^2/2$	0.68×10^{50} erg	ibid
Energy, gravi. $E_{\rm g} = GM_{\rm Bri;vir}^2/r$	1.37×10^{50} erg	$2E_{\rm k} - E_{\rm g} = 0$ (Vrialized)
$t_{\rm ff} = 1/\sqrt{4\pi G\rho}$	0.17 My	
Bubble: Buried SNR		
Centre position $(l, b, v_{\rm LSR})$	$(0^\circ.245,\ 0^\circ.018,\ +30{\rm km\ s^{-1}})$	Figure 9
Radius $r_{\rm bub}$	$0^\circ.0133 = 1.85$ pc	
Mass $M_{\rm bub} = \frac{4\pi r_{\rm bub}^3}{3}\rho_0$	$1.7 \times 10^4 M_\odot$	ρ_0 from virial mass for stable Brick
Expansion velo $v_{\rm expa}$	10 km s^{-1}	
Energy kin. $E_{\rm bub} = (1/2)M_{\rm bub}v_{\rm expa}^2$	0.17×10^{50} erg	
Age (Sedov time) $t_{\rm sed} = (2/5)r_{\rm bub}/v_{\rm expa}$	0.072 My	

$t \sim r/v \sim 3 \times 10^5$ y. If the latter is the case, the mass corresponds to a larger conversion factor of $X_{\rm CO} = 1.6 \times 10^{20}$ H$_2$ cm $^{-2}$ [K km s^{-1}]$^{-1}$, which is closer to the local value (Bolatto et al. 2013).

In either estimates, the mass ($\sim 5 - 6.8 \times 10^4 M_\odot$, table 1) of the Brick derived hear from the CO-line measurement is a factor of three smaller than the current measurement from the dust emission using a gas-to-dust mass ratio of 100, $M_{\rm bub;dust} \sim 1.3 \times 10^5 M_\odot$ (Lis et al. 1991; Lis et al. 1994; Longmore et al. 2012), while the scale radius hear (CO, 2.96 pc) is about the same as current measurements (dust, 2.8 pc). The discrepancy may be solved if the gas-to-dust ratio is reduced to one third, or gas-to-dust ratio in the GC is ~ 30. This would not be unrealistic because of the higher metallicity in the GC, as in the case of $X_{\rm CO}$ (Arimoto et al. 1996).

3.7 Rotating disc

The moment 1 map in figure 2 shows a clear velocity gradient along the major axis (x axis) of the Brick at position angle $\sim 40^\circ$ at $dv/dx \sim 2.5$ km s^{-1}per parsec near the center, which is consistent with that discussed by Henshaw et al. (2019). If the velocity gradient is attributed to the rotation of the Brick along the minor axis, the rotation velocity of the major-axis ends at $r \sim \pm 4$ $(= D_x/2)$ pc is measured to be $V_{\rm rot} \sim 6.5$ km s^{-1}. Then, if the cloud is gravitationally bound against the centrifugal force, the mass of the Brick must be greater than $M_{\rm rot} \sim rV_{\rm rot}^2/G \sim 3.9 \times 10^4 M_\odot$. This mass is smaller than the derived molecular mass, 5.1–6.8$\times 10^4 M_\odot$ (table 1). Therefore, we may consider that the Brick has a disc structure of radius ~ 4 pc, rotating around the minor axis (y axis) at position angle $\sim 130^\circ$, and is gravitationally bound and stable. Namely, the Brick's elongated morphology is explained by an edge-on view of such rotating disc. If this is the case, it affects the estimation of the volume density, so that the density must be about a half of that calculated for a bar shape.

3.8 Radio continuum properties

Figure 8 shows 1.3 GHz radio continuum intensity extracted from the GC survey with the MeerKAT (Heywood et al. 2022) overlaid with 8 μm intensity contours from the Spitzer survey (Churchwell et al. 2009), showing numerous radio filaments. The second panel shows the same, but superposed by ^{13}CO $T_{\rm B}$ map at $v_{\rm LSR}=31$ km s^{-1}by contours every 0.5 K.

Two horn-like filaments parallel to the eastern and western edges of the Brick compose a lobe structure at position angle $\sim 30^\circ$ as traced by the dashed lines A and B, respectively, in the bottom panel. Filament A apparently coincides with the eastern dust arc (Johnston et al. 2014) and the large arc in the molecular-lines (Higuchi et al. 2014; Henshaw et al. 2022). The western filament and enhanced emission in the bubble center as observed at 5 GHz with the VLA (Very Large Array) (Henshaw et al. 2022) are also recognized in this map.

The bottom panel shows the radio spectral index (α) map, which indicates that the filaments and enhancement near the bubble-center are non-thermal with radio spectral index of $\alpha\sim-0.5$ to -0.8. No signature of thermal emission with flat spectrum from HII region is found.

As to physical relation of the non-thermal radio features to the Brick, the following two cases are considered.
i) They are part of an SNR originating in the Brick.
i) They are background GC filaments not related to the Brick.
If (i) is the case, we may estimate the diameter using the surface brightness-diameter ($\Sigma-D$) relation for SNRs (Case & Bhattacharya 1998). $\Sigma_{1.3\ {\rm GHz}}$ of the filaments is read from the radio image to be ~ 2 mJy beam^{-1} for 3.6$''$ synthesized beam. Assuming filament's coverage over the supposed SNR coinciding with the molecular bubble to be on the order of ~ 0.1 and spectral index -0.7, we obtain a rough estimate of radio surface brightness at 1 GHz: $\Sigma_{1\ {\rm GHz}}\sim 6.6\times10^{-21}$ W m^{-2} Hz^{-1} sr^{-1}. Applying the $\Sigma_{\rm 1GHz}-D$ relation (Case & Bhattacharya 1998), we obtain $D\sim 30$ pc. Combining this diameter with the angular diameter of $\sim 1'6$, the distance is estiamted to be ~ 65 kpc, which obviously contradicts the distance to the Brick near the GC. Therefore, We may conclude that case (ii) is more plausible, so that the radio features are not physically associated with the Brick, but are part of the background emission in the Galactic Centre, which is filled with numerous non-thermal filaments (Heywood et al. 2022; Yusef-Zadeh et al. 2022; Sofue 2023).

From the radio map, we may also estimate an upper limit to the thermal emission from the Brick, assuming that the brightness of the thermal emission is less than the brightness fluctuation of the non-thermal emission, or on the order of $\lesssim 0.5$ mJy beam^{-1} at 1.3 GHz. This yields an upper limit to the emission measure as $EM\lesssim 1.6\times10^4$ pc cm^{-6}, whici is less than that for the weakest HII regions in the Galaxy (Downes et al. 1980). This upper limit to the thermal emission is consistent with the negative reports of massive-star formation in the Brick (Longmore et al. 2012; Johnston et al. 2014; Henshaw et al. 2022).

4 Dark SNR buried in the Brick

We have shown that the Brick nests an expanding molecular bubble from the channel maps and position-velocity diagrams, while it is not associated with radio continuum emission indicative of an HII region or an SNR. In this section, we derive the physical parameters of the bubble, and explain it bubble as a dark SNR, or a buried SNR in the dense molecular gas (Sofue 2020; Sofue 2021). We also compare our model with those in the literature.

4.1 Expanding bubble

In figure 3 we showed channel maps of $T_{\rm B}$ in the ^{13}CO line, which exhibited a bubble structure as marked by the red circle. Besides the spatial bubble structure, the position-velocity diagrams in figures 4 and 5 showed elliptical features, which indicates that the bubble is expanding at $v_{\rm exp}\sim 10$ km s^{-1}.

Figure 9 enlarges the channel and position-velocity maps at representative positions and velocities, as marked by the red ellipses, which represent a $(l,b,v_{\rm LSR})$ sphere with radius $0^\circ.0133=1.85$ pc (at 8 kpc distance) centered on $(l,b,v_{\rm LSR})=(0^\circ.245,\ +0^\circ.018,\ +30{\rm km\ s^{-1}})$. The bottom-right panel shows a ^{13}CO line spectrum toward the bubble center, showing a double-peak profile with blue- and red-shifted peaks typical for expanding motion in the line of sight.

We stress that the expansion is nearly symmetric with respect to the bubble's centre not only on the sky but also in the velocity directions. This indicates that the bubble is a closed spherical structure without a break totally embedded in the Brick.

The centre position of the CO bubble is slightly shifted to the south west by ~ 0.6 pc from the geometrical center of the Brick at $(l,b)\simeq(0^\circ.253,+0^\circ.016)$.

The south-eastern edge of the bubble coincides in posi-

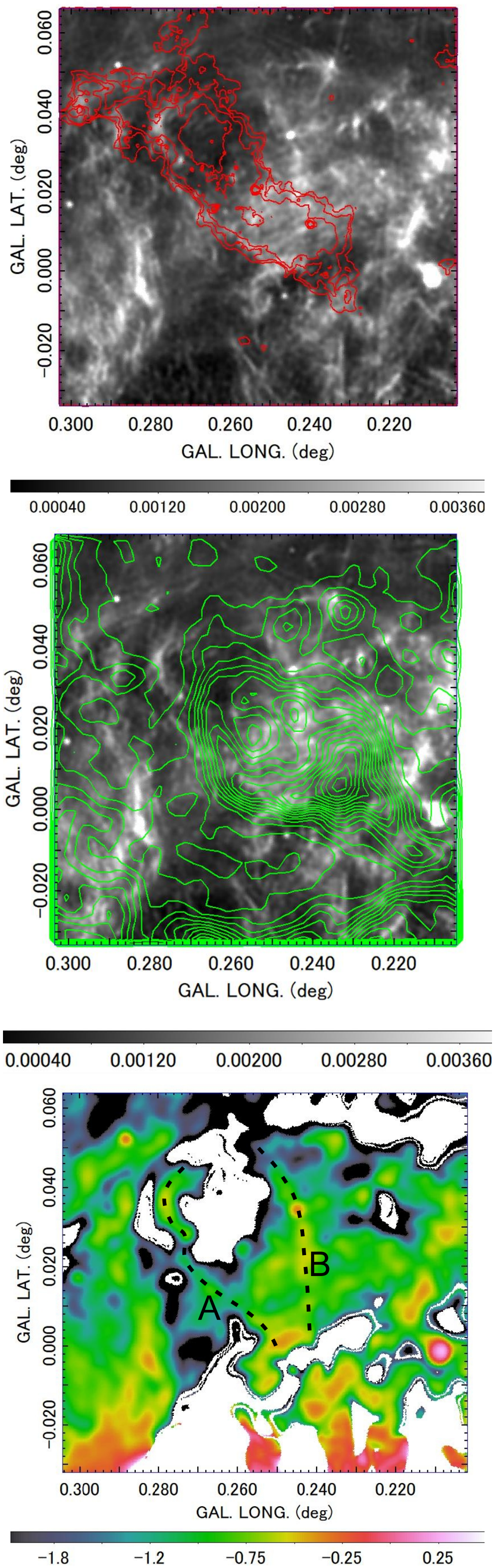

Fig. 8. [Top] 1.3 GHz radio continuum map from MeerKAT (grey scale by bar in Jy/beam) (Heywood et al. 2022; Yusef-Zadeh et al. 2022) with 8 μm contours from 100 (minimum) to 300 every 100 mJy/sr. [Middle] Same, but with ^{13}CO $T_{\rm B}$ contours every 0.5K at $v_{\rm LSR} = 31$ km s^{-1}. [Bottom] Radio spectral index. Dashed lines A and B trace the radio filaments.

tion with the dust arc, whose center is at about the same position as the present CO-bubble's centre (Higuchi et al. 2014; Henshaw et al. 2022).

4.2 Mass and energy of the expanding bubble

Henshaw et al. (2022) have derived the mass of the arcs in the Brick, which coincide with the eastern limb of the present CO-line bubble, to be $M_{\rm arc} \sim 3 \times 10^3 M_\odot$ and kinetic energy of the expanding motion of the arc $E_{\rm k:arc} \sim 7 \times 10^{47}$ and momentum $p_{\rm arc} \sim 1.4 \times 10^4 M_\odot$ km s^{-1}.

We here derive the mass and energy of the bubble from our CO-line data (figure 9). However, it is ambiguous to abstract the mass properly belonging to the bubble from the intensity maps presented in this paper. Therefore, we assume that the bubble is a structure whose mass has been plowed from the cavity, which had approximately the same density as the mean density determined in the previous subsections.

We assume that the Brick is gravitationally stable, and the total mass is equal to the Virial mass, which yielded mean density of $\rho_0 \sim 4.3 \times 10^{-20}$ g cm^{-3} (table 1). The total mass of the bubble is then estimated as

$$M_{\rm bub} \sim \rho_0 (4\pi r^3/3) \sim 1.7 \times 10^4 M_\odot, \tag{12}$$

and the kinetic energy of the expanding motion is

$$E_{\rm kin} \sim 1/2 M_{\rm bub} v_{\rm exp}^2 \sim 1.7 \times 10^{49} {\rm erg}. \tag{13}$$

The derived quantities are listed in table 1.

We point out that the mass and energy of the expanding bubble are smaller than those of the whole Brick by a factor of 4. This means that the bubble is not significantly disturbing the entire structure of the Brick.

4.3 Current models for the bubble

There have been two major ideas to explain the observed arc-shaped properties of the Brick based on interferometric observations of other molecular lines: The cloud-collision model (Higuchi et al. 2014) and stellar-feedback model (Henshaw et al. 2022). The latter may be categorized into cases that take account of expansion of an HII region and stellar wind from central early-type stars.

4.3.1 Cloud-collision model

Cloud-collision model (Higuchi et al. 2014) postulates collision of a compact cloud of mass $\sim 0.5 \times 10^5 M_\odot$ and radius ~ 1.5 pc against a cloud of $\sim 2 \times 10^5 M_\odot$ and ~ 3 pc at velocity of ~ 30–60 km s^{-1}, where the masses are taken from the determination using the dust emission for gas-to-dust mass ratio 100 (Longmore et al. 2012). Difficulty in this

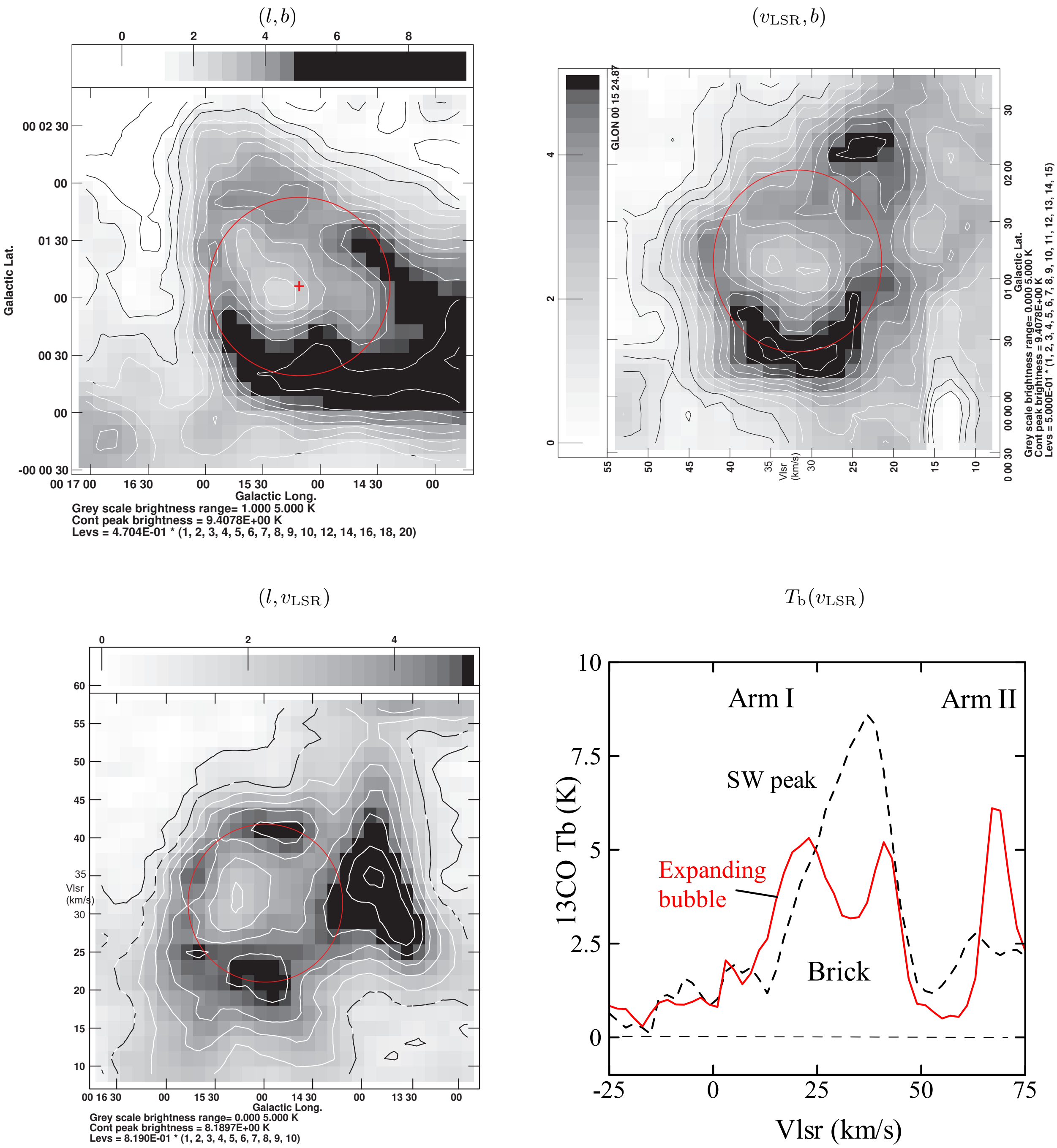

Fig. 9. [Top] ^{13}CO Tb map at $v_{\rm LSR} = 29$ km s^{-1}, showing a spherical shell structure. The circle approximately trace the bubble with radius $r_{\rm bub} = 0^\circ.0132 = 1.84{\rm pc}$ centered on $(l, b) = (0^\circ.245, 0^\circ.018)$ marked with the cross. Bar and contours indicate $T_{\rm B}$ in K. [Top right] $(b, v_{\rm LSR})$ diagram (vertical slice) across the bubble center. Panel is rotated by 90°. [Bottom left] Same, but $(l, v_{\rm LSR})$ (horizontal slice). [Bottom right] ^{13}CO line spectra toward the bubble center (red), showing symmetric expansion in the line of sight. Dashed line shows a peak in the SW corner of top-left panel. Note: Longitude and latitude coordinates are in unit of $dd^\circ\ mm'\ ss''$.

model would be the absence of ionized dense gas (HII region) inevitably created by such high-speed, on-going collision. Another concern is the long mean free path and collision time, which are calculated to be $L_{\rm col} \sim 10$ kpc and $t_{\rm col} = L_{\rm col}/v \sim 200$ Myr, if the CMZ is filled with similar-mass clouds in radius ~ 207 pcand full thickness ~ 56 pc with total molecular mass $2.3 \times 10^7 M_{\odot}$ (Sofue 2022). This collision time is three orders of magnitudes longer than the Jeans time, $t_{\rm J} \sim 7 \times 10^4$ y of the smaller cloud, which leaves a question how the cloud survived for such long time before collision. One more concern is their orbits: why did the colliding cloud come from the halo direction at altitude angle, $\sim 50^{\circ}$, as the morphology of the arc indicates. Also, how was the angular momentum between the two unbound clouds removed in order to make the head-on collision is not explained. Therefore, unless these questions are clarified, we may consider other scenarios for the bubble formation in the Brick.

4.3.2 Stellar-wind model

The wind-blown bubble model postulates a shell structure with molecular mass $\sim 3 \times 10^3 M_{\odot}$, kinetic energy $\sim 7 \times 10^{47}$ erg, and momentum $\sim 1.4 \times 10^4 M_{\odot}$km s^{-1} from the interferometric observations ALMA (Henshaw et al. 2019; Henshaw et al. 2022). Henshaw et al. (2022) suggested two possible scenarios: One is that the arc is formed by thermal pressure of HII gas ionized by the central OB cluster, which is however, ruled out in view of the insufficient amount of UV photons by the adopted model. The other, which the authors prefer, is that the arc is driven by stellar winds from a stellar cluster of $\sim 10^3 M_{\odot}$ in the center, which is hidden behind the dusty cloud. However, the presently derived mass, energy and momentum are an order of magnitude greater than those used in the wind model, which might be difficult to be attributed to the wind model. In the following subsection, we propose a different model, which assumes a supernova explosion in the centre of the Brick.

4.4 Buried SNR model

We here try to explain the observed energy and morphology of the molecular expanding bubble by a buried supernova remnant (SNR) in the Brick. The bubble structure can be approximately traced using the Sedov relation by assuming adiabatic expansion after a point explosion in the cloud:

$$E_0 \sim 1/2 M v^2, \tag{14}$$

where E_0 is the input energy by the SN explosion, $M \sim 4\pi r^3 \rho_0/3$ is plowed gas on the shell, $v = dr/dt$ is the expansion velocity, and ρ_0 is the ambient density of the ISM. The relation is equivalent to the Sedov's solution, and reduces to

$$v = dr/dt \sim a\ r^{-3/2}, \tag{15}$$

and is solved to give the radius as a function of time,

$$r \sim b\ t^{2/5}, \tag{16}$$

and the age by the radius and velocity,

$$t \sim (2/5) r/v. \tag{17}$$

Here, $a = [2E_0/(4\pi\rho_0)]^{1/2}$ and $b = (5/2)^{2/5} a^{2/5} = 1.256 (E_0/\rho_0)^{1/5}$ are constants. Inserting $v = 10.0$ km s^{-1}, $r = 1.85$ pc, we obtain $t \sim 7.2 \times 10^4$ y.

We recall that the gas density in the Brick is four orders of magnitudes higher than that in the interstellar space, where the majority of the known SNRs of shell type have been discovered. However, equations (15) and (16) indicate that the SNR in the present circumstance evolves much more quickly that the emission phase was over in the early stage ($t \lesssim 10^{2-3}$ y) by exhausting the energy by strong thermal emission of the ionized gas with cooling rate proportional to the square of the gas density (Shull 1980; Wheeler et al. 1980). After the bubble cooled down and became radio quiet, the shell is still expanding with the kinetic energy and momentum being conserved, as observed.

Although the explosion may have somehow disturbed the Brick structure, since the kinetic energy of the expanding motion is several times smaller than the gravitational energy of the Brick, the SN explosion does not disturb the gravitational stability of the cloud.

5 Summary

We obtained detailed kinematics and energetics of the GC Brick G0.253+0.016+30 km s^{-1}analyzing the CO-line data obtained by the Nobeyama 45-m mm wave telescope. Detailed inspection into the longitude-velocity diagrams in the CO line emission indicates that the Brick may be located inside the CMZ, but in front of the GC, associated with the GC Arm I. This puts the Brick at a distance of 8 kpc, about 0.2 kpc in front of the GC, rather than at a distance of 7.2 kpc away from GC by 1 kpc as currently suggested by infrared photometry.

We have shown that the Brick, G0.253+0.016, is a dense molecular cloud with Virial mass of $M_{\rm Bri;vir} \sim 6.8 \times 10^4 M_{\odot}$ and gravitational energy $E_{\rm g} \sim 1.37 \times 10^{50}$ erg, and kinetic energy $E_{\rm k} \sim 0.68 \times 10^{50}$ erg. By adopting the Virial mass for the molecular gas mass, we obtain a new CO-to-H$_2$ conversion factor of $X_{\rm CO;Bri} \sim 1.3 \times 10^{20}$ H$_2$ cm $^{-2}$ [K km

$\mathrm{s}^{-1}]^{-1}$.

It was shown that the cloud's center is a cavity surrounded by a dense molecular-gas bubble, which is expanding at $v_{\rm expa} = 10$ km s^{-1}with kinetic energy of $E_{\rm k,bub} \sim 1.7 \times 10^{49}$ erg. However, the bubble does not nest a radio continuum SNR or HII regions, and hence it is not associated with massive star formation (Higuchi et al. 2014). We argue that the bubble may be a dark SNR (dSNR) buried in the Brick, whose emission phase was over, but is expanding by the energy and momentum conservation, similar to the dSNRs currently discovered in dense molecular clouds in the Galactic disc (Sofue 2020; Sofue 2021). Approximating the evolution by the Sedov's solution, the age is estimated to be 7×10^4 y. The Brick is, therefore, not a star formation-less system, but there was an activity to form a massive star in the past associated with a supernova explosion in the center

Acknowledgments

The data analysis was performed at the Astronomical Data Analysis Center of the National Astr. Obs. of Japan. The author thanks Dr. Tomoharu Oka for the Nobeyama, Dr. H. Churchwell for Spitzer, and Drs. I. Heywood and F. Yusef-Zadeh for MeerKAT archival data. The author is indebted to the referee for the valuable comments and suggestions to prove the paper.

Data availability

The CO data were taken from https://www.nro.nao.ac.jp/ ∼nro45mrt/html/ results/data.html. Spitzer FIR image was downloaded from: https://irsa.ipac.caltech.edu/data/SPITZER/GLIMPSE/

Conflict of interest

There is no conflict of interest.

References

Anderson, L. D., Bania, T. M., Balser, D. S., et al. 2014, ApJS, 212, 1.
Arimoto, N., Sofue, Y., & Tsujimoto, T. 1996, PASJ, 48, 275.
Bolatto, A. D., Wolfire, M., & Leroy, A. K. 2013, ARA&A, 51, 207.
Case, G. L., Bhattacharya, D. 1998, ApJ, 504, 761.
Churchwell, E., Babler, B. L., Meade, M. R., et al. 2009, PASP, 121, 213.
Dame, T. M., Hartmann, D., & Thaddeus, P. 2001, ApJ, 547, 792.
Downes, D., Wilson, T. L., Bieging, J., et al. 1980, A&AS, 40, 379
Ginsburg, A., Barnes, A. T., Battersby, C. D., et al. 2023, ApJ, 959, 36.
Guesten, R. & Henkel, C. 1983, AA, 125, 136
Henshaw, J. D., Ginsburg, A., Haworth, T. J., et al. 2019, MNRAS, 485, 2457.
Henshaw, J. D., Krumholz, M. R., Butterfield, N. O., et al. 2022, MNRAS, 509, 4758.
Heywood, I., Rammala, I., Camilo, F., et al. 2022, ApJ, 925, 165.
Johnston, K. G., Beuther, H., Linz, H., et al. 2014, AA, 568, A56.
Higuchi, A. E., Chibueze, J. O., Habe, A., et al. 2014, AJ, 147, 141.
Lis, D. C., Carlstrom, J. E., & Keene, J. 1991, ApJ, 380, 429.
Lis, D. C., Menten, K. M., Serabyn, E., et al. 1994, ApJL, 423, L39.
Lis, D. C. & Carlstrom, J. E. 1994, ApJ, 424, 189.
Longmore, S. N., Rathborne, J., Bastian, N., et al. 2012, ApJ, 746, 117.
Martínez-Arranz, Á., Schödel, R., Nogueras-Lara, F., et al. 2022, AA, 660, L3.
Shull, J. M. 1980, ApJ, 237, 769.
Sofue, Y. 1995, PASJ, 47, 551.
Sofue, Y. 2013, PASJ, 65, 118.
Sofue, Y. 2020, PASJ, 72, L11.
Sofue, Y. 2021, Galaxies, 9, 13.
Sofue, Y. 2022, MNRAS, 516, 907.
Sofue, Y. 2023, MNRAS, 518, 6273.
Tokuyama, S., Oka, T., Takekawa, S., et al. 2019, PASJ, 71, S19. j, 69, 78.
Walker, D. L., Longmore, S. N., Bally, J., et al. 2021, MNRAS, 503, 77.
Wenger, T. V., Balser, D. S., Anderson, L. D., et al. 2023, VizieR Online Data Catalog, J/ApJ/887/114.
Wheeler, J. C., Mazurek, T. J., & Sivaramakrishnan, A. 1980, ApJ, 237, 781.
Yusef-Zadeh, F., Arendt, R. G., Wardle, M., et al. 2022, ApJL, 925, L18.
Zoccali, M., Valenti, E., Surot, F., et al. 2021, MNRAS, 502, 1246.